Higgs Production at NNLL′+NNLO using Rapidity Dependent Jet Vetoes

Shireen Gangal,[a] **Jonathan R. Gaunt,**[b] **Frank J. Tackmann,**[c] **and Eleni Vryonidou**[b]

[a] *Tata Institute of Fundamental Research, Mumbai 400005, India*

[b] *CERN Theory Division, 1211 Geneva 23, Switzerland*

[c] *Theory Group, Deutsches Elektronen-Synchrotron (DESY), D-22607 Hamburg, Germany*

E-mail: shireen.gangal@theory.tifr.res.in,
jonathan.richard.gaunt@cern.ch, frank.tackmann@desy.de,
eleni.vryonidou@cern.ch

ABSTRACT: The rapidity-dependent jet veto observables $\mathcal{T}_{Bj}$ and $\mathcal{T}_{Cj}$ provide a tight jet veto at central rapidity, gradually transitioning to a loose veto at forward rapidities. They divide the phase space into exclusive jet bins in a different way to the traditional jet veto observable p_{Tj}, and are advantageous to use under harsh pile-up conditions. We obtain predictions for the 0-jet gluon-fusion (ggF) Higgs cross section using both of these veto observables at NNLL′+NNLO, and compare these predictions to the prior state-of-the-art of NLL′+NLO. A significant reduction in perturbative uncertainty is observed going from NLL′+NLO to NNLL′+NNLO, with the NNLL′+NNLO predictions lying inside the uncertainty band of the NLL′+NLO predictions. We also investigate the relative sensitivities of ggF Higgs cross sections with $\mathcal{T}_{Bj}$, $\mathcal{T}_{Cj}$ and p_{Tj} jet vetoes to underlying event and hadronisation effects using an NLO+parton shower calculation. We find that the cross sections with $\mathcal{T}_{Bj}$ and $\mathcal{T}_{Cj}$ vetoes have a reduced sensitivity to underlying event and hadronisation effects compared to that with a p_{Tj} veto.

Contents

1 Introduction

Jet vetoes find frequent application at the LHC, to separate different types of hard processes and cut away backgrounds. One key process where jet vetoes find application is in Higgs production – for example, in the $H \to WW^*$ analysis, it is standard to apply a jet veto to reduce the dominant $t\bar{t}$ decay background.

For maximal background rejection, it is typically advantageous to set the jet veto scale $\mathcal{T}^{\rm cut}$ to be much smaller than the hard scale of the process Q. This induces large logarithms of $\mathcal{T}^{\rm cut}/Q$ in the perturbative series for the 0-jet cross section, which can be summed up to all orders to obtain precise predictions [1, 2].

The standard jet variable by which jets are currently classified and vetoed is the transverse momentum p_{Tj} of a jet. One identifies all jets with a given radius R in an event, computes p_{Tj} for each jet, and vetoes the event if the p_{Tj} for any jet exceeds the veto scale $p_{Tj}^{\rm cut}$. Predictions for the 0-jet Higgs production cross section with a jet veto imposed via p_{Tj} have been obtained with a resummation of p_{Tj}/m_H logarithms up to the NNLL$'$ order, matched to either NNLO or N^{3}LO fixed order perturbation theory [3–8]. However, there are some drawbacks to using this variable. In harsh pile-up conditions, as are nowadays encountered at the LHC, it is hard to identify (and veto) jets with small p_{Tj} at large rapidity. This is due to the lack of tracking information at large $|\eta_j| \geq 2.5$, meaning that at large rapidities it is difficult to disentangle small p_{Tj} jets from the primary process from pile-up jets. One option is simply to raise the overall cut on p_{Tj}, but then the discriminating power of the jet veto is reduced. An alternative possibility is to consider a step-like jet veto, with a tight veto below some value of $|\eta|$, and a weaker veto above this value. The theoretical description of such step-like vetoes is discussed in Ref. [9].

A final possibility, proposed in Refs. [10, 11] and which we focus on here, is to have a jet veto that is a smooth function of rapidity, being tight at central rapidities and gradually weakening as one goes forward. Four jet-veto variables of this kind were considered in Ref. [11]:

$$\mathcal{T}_{Bj} = m_{Tj} e^{-|y_j - Y|} \qquad\qquad \mathcal{T}_{Cj} = \frac{m_{Tj}}{2\cosh(y_j - Y)} \qquad (1.1)$$

$$\mathcal{T}_{Bj\text{cm}} = m_{Tj} e^{-|y_j|} \qquad\qquad \mathcal{T}_{Cj\text{cm}} = \frac{m_{Tj}}{2\cosh(y_j)} \qquad (1.2)$$

where y_j the rapidity of the jet and Y the rapidity of the Higgs. The transverse mass of the jet $m_{Tj} = \sqrt{m_j^2 + p_{Tj}^2}$ and is close to p_{Tj} for small jet radius R. The quantity $\mathcal{T}_{Bj(\text{cm})}$ has the same rapidity weighting as the global beam thrust hadronic event shape [1, 12], whilst $\mathcal{T}_{Cj(\text{cm})}$ has the same rapidity weighting as the C-parameter defined for $e^+ e^- \to$ hadrons. Resummation of veto logarithms for all of these observables can be achieved using the same framework (see Ref. [11] for details).

The veto observables in Eqs. (1.1) and (1.2) are closely linked, differing only in their reference point from which to define whether jets are 'central' and 'forward'; the observables in Eq. (1.1) do it with respect to the Higgs rapidity, whilst those in Eq. (1.2) do it with respect to the centre of momentum of the pp collision. In terms of avoiding the issues with forward pile-up jets, the latter alternative will be superior, although there should not be a drastic difference in performance between the two types of vetoes at the LHC, since the majority of Higgs bosons are produced at rather low rapidities. Here, we choose to focus on the observables in Eq. (1.1), motivated in part by the fact that these seem to be the preferred choice from an experimental perspective: in Ref. [13] the $H + 0$-jet cross section differential in $\mathcal{T}_{Cj}$ was measured in the ATLAS $H \to \gamma\gamma$ analysis.

Apart from the above considerations, given the general utility of jet binning it is clearly beneficial to have more than one way of dividing phase space up into jet bins – for certain analyses it may be advantageous to use $\mathcal{T}_{B/Cj}$ rather than p_{Tj}. Vetoed cross sections using $\mathcal{T}_{B/Cj}$ probe QCD radiation in a quite different way from cross sections with a p_{Tj} veto[1], so studying and measuring these observables is also of interest in terms of testing our understanding of QCD radiation.

The factorisation framework to resum veto logarithms for colour-singlet 0-jet processes with a jet veto imposed via $\mathcal{T}_{B/Cj}$ was established in Ref. [10, 11] within soft collinear effective theory (SCET). For the gluon-fusion (ggF) Higgs cross section, predictions for the 0-jet cross section with a $\mathcal{T}_{B/Cj}$ jet veto have been obtained at NLL′+NLO [11]. In Ref. [14], the resummation ingredients (two-loop beam and soft functions) required for the NNLL′ resummation of colour-singlet 0-jet processes with a $\mathcal{T}_{B/Cj}$ jet veto were computed.

The main goal of the present paper is to elevate the precision of the 0-jet ggF Higgs production predictions, for both $\mathcal{T}_{Bj}$ and $\mathcal{T}_{Cj}$ to NNLL′ in resummed logarithms of $\mathcal{T}_{B/Cj}/m_H$, matched to NNLO fixed-order perturbation theory. We will include finite bottom and top

---

[1]Technically: p_{Tj} veto cross sections are SCET$_{\text{II}}$ observables whilst $\mathcal{T}_{B/Cj}$ veto cross sections are SCET$_{\text{I}}$ observables.

quark mass effects up to two loops (NLO) in the Higgs production process, and resum time-like logarithms in the $gg \to H$ form factor to all orders [15–20]. Note that here we do not perform a resummation of logarithms of R (studied in Refs. [8, 21–23]), nor logarithms of m_b/m_H (studied in Refs. [24–26]).

A further goal is to investigate the relative sensitivity of the 0-jet ggH cross sections with $\mathcal{T}_{Bj}$, $\mathcal{T}_{Cj}$ and p_{Tj} vetoes to the effects of hadronisation and underlying event (UE). These effects are difficult to describe from first principles and are typically modelled, so a minimal sensitivity to them is preferable. This investigation will be performed using a NLO + parton shower (PS) set-up, specifically MADGRAPH_AMC@NLO [27] + Pythia8 [28]. We find that the cross sections with $\mathcal{T}_{Bj}$ and $\mathcal{T}_{Cj}$ vetoes are rather less sensitive to both UE and hadronisation than that with a p_{Tj} veto, which constitutes another advantage of using these veto observables.

This paper is organised as follows. In section 2 we review the SCET factorization formula derived in Refs. [10, 11] for the $H + 0$-jet $\mathcal{T}_{B/Cj}$ cross section, and outline the steps and necessary ingredients needed to obtain this cross section at NNLL′+NNLO. In section 3 we give details of the procedure we use to determine the perturbative uncertainty in our results. Section 4 contains our results for the $H + 0$-jet $\mathcal{T}_{B/Cj}$ cross section at NNLL′+NNLO, and we investigate the effects of UE and hadronisation on the $H + 0$-jet $\mathcal{T}_{B/Cj}$ and p_{Tj} cross sections using an NLO+PS set-up in section 5. Finally we conclude in section 6.

2   Factorization for the $H + 0$-jet cross section

The full $pp \to H + 0$-jet cross section with a cut on the rapidity-dependent observable $\mathcal{T}_{fj} < \mathcal{T}^{\mathrm{cut}}$ ($f = B, C$) is given by,

$$\sigma_0(\mathcal{T}_{fj} < \mathcal{T}^{\mathrm{cut}}) = \sigma_0^{\mathrm{resum}}(\mathcal{T}_{fj} < \mathcal{T}^{\mathrm{cut}}) + \sigma_0^{\mathrm{nons}}(\mathcal{T}_{fj} < \mathcal{T}^{\mathrm{cut}}), \tag{2.1}$$

where the first term contains the resummed logarithms of $\mathcal{T}^{\mathrm{cut}}/m_H$, and dominates for small values of $\mathcal{T}^{\mathrm{cut}}$, while the second term contains the nonsingular corrections which are suppressed by $O(\mathcal{T}^{\mathrm{cut}}/m_H)$ and become important at large $\mathcal{T}^{\mathrm{cut}}$. The resummed $H+0$-jet cross section for $\mathcal{T}_{fj} < \mathcal{T}^{\mathrm{cut}}$ can be factorized as follows, [10, 11]

$$\sigma_0^{\mathrm{resum}}(\mathcal{T}_{fj} < \mathcal{T}^{\mathrm{cut}}) = \sigma_B H_{gg}(m_t, m_b, m_H^2, \mu)\, B_g(m_H \mathcal{T}^{\mathrm{cut}}, x_a, R, \mu) B_g(m_H \mathcal{T}^{\mathrm{cut}}, x_b, R, \mu)$$
$$\times\, S_f(\mathcal{T}^{\mathrm{cut}}, R, \mu) + \sigma_0^{\mathrm{Rsub}}(\mathcal{T}_{fj} < \mathcal{T}^{\mathrm{cut}}, R), \tag{2.2}$$

where

$$x_{a,b} = \frac{m_H}{E_{\mathrm{cm}}}\, e^{\pm Y}, \quad \sigma_B = \frac{\sqrt{2} G_F\, m_H^2}{576\pi E_{\mathrm{cm}}^2}. \tag{2.3}$$

The hard function denoted by H_{gg} contains the hard virtual corrections and is obtained by matching QCD onto the operator O_{ggH} in SCET. The gluon beam function B_g describes the collinear initial state radiation from the incoming gluons, while S_f encodes the contribution

from the soft radiation across the entire event. The term σ_0^{Rsub} contains $O(R^2)$ corrections arising due to the clustering of two independent collinear or soft particles into one jet; following Refs. [7, 10] we separate these off and treat them separately[2].

The hard function is the IR-finite part of the $\overline{\text{MS}}$ renormalized ggH form factor, and is expressed in terms of the matching coefficient C_{ggH} as,

$$H_{gg}(m_t, m_b, m_H^2, \mu) = |C_{ggH}(m_t, m_b, m_H^2, \mu)|^2 . \tag{2.4}$$

At NNLL$'$, we require the hard function up to NNLO:

$$\begin{aligned} H_{gg} =& |C_{ggH}^{(0)}|^2 + \frac{\alpha_s(\mu)}{4\pi} 2\text{Re}\left[C_{ggH}^{(1)} C_{ggH}^{(0)*}\right] \\ &+ \frac{\alpha_s^2(\mu)}{(4\pi)^2}\left(2\text{Re}\left[C_{ggH}^{(2)} C_{ggH}^{(0)*}\right] + |C_{ggH}^{(1)}|^2\right) + ..., \end{aligned} \tag{2.5}$$

where the $C_{ggH}^{(0,1,2)}$ are the perturbative expansion coefficients of C_{ggH}:

$$C_{ggH} = C_{ggH}^{(0)} + \frac{\alpha_s}{4\pi} C_{ggH}^{(1)} + \left(\frac{\alpha_s}{4\pi}\right)^2 C_{ggH}^{(2)} + ... \tag{2.6}$$

Note that since C_{ggH} begins at $\mathcal{O}(\alpha_s)$ we absorb one power of α_s into each coefficient $C_{ggH}^{(0,1,2)}$.

In $C^{(0)}$ and $C^{(1)}$ we include the top and bottom loops with the full mass dependence using the results of Refs. [29, 30]. For the NNLO coefficient $C^{(2)}$, we use the NNLO $m_t \to \infty$ result extracted from Refs. [31, 32], reweighted by the ratio of $C^{(0)}$ with finite m_t to $C^{(0)}$ with $m_t \to \infty$ (both with $m_b = 0$). This approach to the NNLO term is the same as in Ref. [2].

The beam functions B_g are the same for both the $\mathcal{T}_{Bj}$ and $\mathcal{T}_{Cj}$ observables as they describe collinear emissions in the regions of large forward rapidities where the measurement function for both these observables is the same. They can be computed as a convolution between the perturbative matching kernel $\mathcal{I}_{ij}$ and the standard parton distribution functions (PDFs) as follows [1, 33],

$$B_g(t^{\text{cut}}, x, R, \mu) = \sum_j \int_x^1 \frac{dz}{z} \mathcal{I}_{gj}(t^{\text{cut}}, z, R, \mu) f_j\left(\frac{x}{z}, \mu\right) \times \left[1 + \mathcal{O}\left(\frac{\Lambda_{\text{QCD}}^2}{t^{\text{cut}}}\right)\right]. \tag{2.7}$$

For NNLL$'$ precision we require the matching kernel up to $\mathcal{O}(\alpha_s^2)$:

$$\mathcal{I}_{gj}(t, z, \mu) = \mathcal{I}_{gj}^{(0)}(t^{\text{cut}}, x, \mu) + \frac{\alpha_s(\mu)}{4\pi} \mathcal{I}_{gj}^{(1)}(t^{\text{cut}}, x, \mu) + \frac{\alpha_s^2(\mu)}{(4\pi)^2} \mathcal{I}_{gj}^{(2)}(t^{\text{cut}}, x, \mu, R) + \mathcal{O}(\alpha_s^3) . \tag{2.8}$$

---

[2]This scheme is the second one discussed in section 3.2 of Ref. [14]. This implies that in the two-loop B and S, we do not include the $\Delta I_{\text{indep}}, SC$ and $\Delta S_{f,\text{indep}}$ terms computed in Ref. [14], and remove the $C_A^2 R^2$ term associated with independent emission contributions from the anomalous dimensions of B and S.

The one-loop coefficients $\mathcal{I}^{(1)}$ are given in Ref. [11] and are equal to the cumulants of the one-loop virtuality-dependent beam function matching coefficients computed in Ref. [2]. One can write the two-loop coefficients $\mathcal{I}^{(2)}$ as follows:

$$\mathcal{I}_{gj}^{(2)}(t^{\text{cut}}, x, \mu, R) = \mathcal{I}_{G,gj}^{(2)}(t^{\text{cut}}, x, \mu) + \Delta\mathcal{I}_{gj}^{(2)}(t^{\text{cut}}, x, \mu, R) \tag{2.9}$$

where the $\mathcal{I}_G^{(2)}$ are the cumulants of the two-loop virtuality-dependent beam function matching coefficients computed in Ref. [34], and the expressions for $\Delta\mathcal{I}^{(2)}$ are given in section 3.1.2 of Ref. [14].

The soft function is defined as a vacuum matrix element of the product of soft Wilson lines along the two incoming gluon directions, with a measurement function imposing $\mathcal{T}_{fj} < \mathcal{T}^{\text{cut}}$. As with the other ingredients, we require its expansion to NNLO:

$$S_f(\mathcal{T}^{\text{cut}}, R, \mu) = 1 + \frac{\alpha_s(\mu)}{4\pi} S_f^{(1)}(\mathcal{T}^{\text{cut}}, \mu) + \frac{\alpha_s^2(\mu)}{(4\pi)^2} S_f^{(2)}(\mathcal{T}^{\text{cut}}, R, \mu) + \mathcal{O}(\alpha_s^3) \tag{2.10}$$

The one-loop soft functions $S_f^{(1)}$ for $\mathcal{T}_{Bj}$ and $\mathcal{T}_{Cj}$ are equal to the cumulants of the one-loop soft functions for thrust and C-parameter respectively; the expressions for both observables are given in Ref. [11]. Let us decompose the two-loop soft function as follows:

$$S_f^{(2)}(\mathcal{T}^{\text{cut}}, R, \mu) = S_{G,f}^{(2),\text{non-Ab}}(\mathcal{T}^{\text{cut}}, R, \mu) + \frac{1}{2}\left[S_f^{(1)}(\mathcal{T}^{\text{cut}}, \mu)\right]^2 + \Delta S_f^{(2)}(\mathcal{T}^{\text{cut}}, R, \mu) \tag{2.11}$$

The quantity $S_{G,f}^{(2),\text{non-Ab}}$ is the cumulant of the 'non-Abelian' part of the two-loop thrust/C-parameter soft function. Expressions for $\Delta S_f^{(2)}$ are given in section 3.1.1 of Ref. [14]. Analytic results for $S_{G,B}^{(2),\text{non-Ab}}$ can be extracted from the results in Refs. [35–38], whilst for $S_{G,C}^{(2),\text{non-Ab}}$ we extracted numerical results for $n_f = 5$ from Ref. [39]. In both cases the results are of the form:

$$S_{G,f}^{(2),\text{non-Ab}} = a_{G,f}C_A + b_{G,f}C_A \ln\left(\frac{\mathcal{T}^{\text{cut}}}{\mu}\right) - \frac{8}{9}C_A\left(67C_A - 3C_A\pi^2 - 20n_fT_F\right)\ln\left(\frac{\mathcal{T}^{\text{cut}}}{\mu}\right)^2$$

$$+ \frac{16}{9}C_A\left(11C_A - 4n_fT_F\right)\ln\left(\frac{\mathcal{T}^{\text{cut}}}{\mu}\right)^3 \tag{2.12}$$

where $a_{G,f}$ and $b_{G,f}$ are given by:

$$a_{G,C}|_{n_f=5} = 124.075 \tag{2.13}$$

$$b_{G,C}|_{n_f=5} = -265.650 \tag{2.14}$$

$$a_{G,B} = \frac{1}{810}\left[20n_fT_F(40 + 111\pi^2 - 1044\zeta_3) + C_A(-21400 - 5025\pi^2 + 396\pi^4 + 57420\zeta_3)\right] \tag{2.15}$$

$$b_{G,B} = -\frac{4}{27}\left[n_fT_F(112 - 12\pi^2) + C_A(33\pi^2 - 404 + 378\zeta_3)\right] \tag{2.16}$$

Numerical results for the two-loop soft functions $S_f^{(2)}(\mathcal{T}^{\mathrm{cut}}, R, \mu)$ have also been obtained using SoftSERVE [40–42], where these results agree with those obtained using the procedure above.

The hard, beam and soft functions are evaluated at their natural scales $\mu_H \sim m_H$, $\mu_B \sim \sqrt{m_H \mathcal{T}^{\mathrm{cut}}}$ and $\mu_S \sim \mathcal{T}^{\mathrm{cut}}$, to minimize the logarithms they contain, and then RG evolved to a common scale $\mu_{\mathrm{FO}} \sim m_H$ which sums the large logarithms. These satisfy RG equations with a multiplicative form due to the cumulant nature of the jet veto observables [10]:

$$
\begin{aligned}
\mu \frac{\mathrm{d}}{\mathrm{d}\mu} \ln\big[C_{ggH}(m_t, m_H^2, \mu)\big] &= \gamma_H^g(m_H^2, \mu)\,, \\
\mu \frac{\mathrm{d}}{\mathrm{d}\mu} \ln\big[B_g(t^{\mathrm{cut}}, x, R, \mu)\big] &= \gamma_B^g(t^{\mathrm{cut}}, R, \mu)\,, \\
\mu \frac{\mathrm{d}}{\mathrm{d}\mu} \ln\big[S_g^{B,C}(\mathcal{T}^{\mathrm{cut}}, R, \mu)\big] &= \gamma_S^g(\mathcal{T}^{\mathrm{cut}}, R, \mu)\,,
\end{aligned}
\tag{2.17}
$$

where the anomalous dimension has a generic form consisting of the μ-dependent cusp part and the non-cusp part as follows,

$$
\begin{aligned}
\gamma_H^g(m_H^2, \mu) &= \Gamma_{\mathrm{cusp}}^g[\alpha_s(\mu)] \ln \frac{-m_H^2 - \mathrm{i}0}{\mu^2} + \gamma_H^g[\alpha_s(\mu)]\,, \\
\gamma_B^g(t^{\mathrm{cut}}, R, \mu) &= -2\Gamma_{\mathrm{cusp}}^g[\alpha_s(\mu)] \ln \frac{t^{\mathrm{cut}}}{\mu^2} + \gamma_B^g[\alpha_s(\mu), R]\,, \\
\gamma_S^g(\mathcal{T}^{\mathrm{cut}}, R, \mu) &= 4\Gamma_{\mathrm{cusp}}^g[\alpha_s(\mu)] \ln \frac{\mathcal{T}^{\mathrm{cut}}}{\mu} + \gamma_S^g[\alpha_s(\mu), R]\,.
\end{aligned}
\tag{2.18}
$$

The hard matching coefficient contains double logarithms of $(-m_H^2 - \mathrm{i}0)/\mu_H^2$, so we choose $\mu_H \sim -\mathrm{i}m_H$ in order to avoid large left over logarithms $\ln^2(-1 - \mathrm{i}0) = -\pi^2$. Choosing an imaginary hard scale ensures that the logarithms are fully resummed and results in better perturbative convergence. For NNLL' resummation we require the cusp anomalous dimension Γ_{cusp} up to 3 loops, and the non-cusp anomalous dimensions up to 2 loops. The expression for the former is given, for example, in Ref. [2] (using the results of Refs. [43, 44]). The two-loop expression for $\gamma_H^g[\alpha_s(\mu)]$ can be found in the same paper (using the results of Refs. [45–47]). The dependence on jet radius enters through the two-loop non-cusp anomalous dimension of the beam and soft function, which can be split into a global and an R-dependent part,

$$
\begin{aligned}
\gamma_S^g[\alpha_s(\mu), R] &= \gamma_{G,S}^g[\alpha_s(\mu)] + \Delta\gamma_S^g[\alpha_s(\mu), R] \\
\gamma_B^g[\alpha_s(\mu), R] &= \gamma_{G,B}^g[\alpha_s(\mu)] + \Delta\gamma_B^g[\alpha_s(\mu), R]
\end{aligned}
\tag{2.19}
$$

The global non-cusp anomalous dimensions $\gamma_{G,S}^g[\alpha_s(\mu)]$ and $\gamma_{G,B}^g[\alpha_s(\mu)]$ are those of the beam thrust soft and beam functions, and are given up to 2 loops in Ref. [2]. The R-dependent correction term for the soft function anomalous dimension, $\Delta\gamma_S^g[\alpha_s(\mu), R]$, is given in section 3.1.1 of Ref. [14]; RGE consistency demands $\Delta\gamma_B^g[\alpha_s(\mu), R] = -\frac{1}{2}\Delta\gamma_S^g[\alpha_s(\mu), R]$.

The solution of the RGE (Eq. (2.17)) has a similar structure for the hard, beam and soft functions. For the beam function, solving the RGE yields,

$$B_g(t^{\mathrm{cut}}, x, R, \mu) = U_B(t^{\mathrm{cut}}, \mu_B, \mu) \, B_g(t^{\mathrm{cut}}, x, R, \mu_B) \tag{2.20}$$

with the evolution factor given by

$$U_B(t^{\mathrm{cut}}, \mu_B, \mu) = e^{K_B(\mu_B, \mu)} \Big(\frac{t^{\mathrm{cut}}}{\mu_B^2}\Big)^{\eta_B(\mu_B, \mu)} . \tag{2.21}$$

Explicit expressions for the evolution of the hard and soft functions along with the various factors relevant for the resummation at NNLL$'$ can be found in Refs. [2, 11].

The contribution σ_0^{Rsub} in Eq. (2.2) takes account of the $\mathcal{O}(R^2)$ corrections for the clustering of independent emissions. The form of this term is as follows [4, 7, 14]:

$$
\begin{aligned}
\sigma_0^{\mathrm{Rsub}} =& \frac{\alpha_s^2(\mu_{\mathrm{avg}})}{(4\pi)^2} H_{gg}^{(0)} \, U_{\mathrm{total}}(\mathcal{T}^{\mathrm{cut}}, \mu_H, \mu_B, \mu_S, \mu_{\mathrm{FO}}) \times \\
& \Big[\Big\{ f_g(x_a, \mu_B) \, f_j(x_b, \mu_B) \otimes \Big(\Delta I_{gj,\mathrm{indep}}^{(2)}(x_b, \mu_{\mathrm{avg}}, R) + SC_{gj}^{(2)}(x_b, \mu_{\mathrm{avg}}, R) \Big) + (x_a \leftrightarrow x_b) \Big\} \\
& + f_g(x_a, \mu_B) \, f_g(x_b, \mu_B) \, \Delta S_{f,\mathrm{indep}}^{(2)}(\mathcal{T}^{\mathrm{cut}}, \mu_{\mathrm{avg}}, R) \Big]
\end{aligned}
\tag{2.22}
$$

where

$$U_{\mathrm{total}}(\mathcal{T}^{\mathrm{cut}}, \mu_H, \mu_B, \mu_S, \mu) = U_S(\mathcal{T}^{\mathrm{cut}}, \mu_S, \mu) \times U_B^2(m_H \mathcal{T}^{\mathrm{cut}}, \mu_B, \mu) \times U_H(\mu_H, \mu) \tag{2.23}$$

is the total NNLL$'$ evolution kernel, and $\mu_{\mathrm{avg}} = \sqrt{\mu_B \mu_S}$. Since the $\mathcal{O}(\alpha_s^2)$ corrections in the square brackets come from soft or collinear emissions, we choose to evaluate them at the geometric mean of the soft and beam scales, as in Ref. [7]. The expressions for these corrections can be found in section 3.2 of Ref. [14].

The nonsingular cross section computed at fixed order up to NNLO at scale μ_{FO} can be obtained by expanding Eq. (2.1) up to NNLO with all scales set to μ_{FO}. In Eq. (2.2) we expand the product of fixed order contributions to the H, B and S factors to $\mathcal{O}(\alpha_s^2)$, such that setting all scales to μ_{FO} automatically results in the NNLO expansion. Thus:

$$
\begin{aligned}
\sigma_0^{\mathrm{nons,NNLO}}(\mathcal{T}_{fj} < \mathcal{T}^{\mathrm{cut}}, \mu_{\mathrm{FO}}) =& \sigma_0^{\mathrm{FO,NNLO}}(\mathcal{T}_{fj} < \mathcal{T}^{\mathrm{cut}}) \\
& - \sigma_0^{\mathrm{resum,NNLL}'}(\mathcal{T}_{fj} < \mathcal{T}^{\mathrm{cut}}, \mu_B = \mu_S = \mu_H = \mu_{\mathrm{FO}}),
\end{aligned}
\tag{2.24}
$$

We compute the first term on the right hand side at NNLO as follows:

$$\sigma_0^{\mathrm{FO,NNLO}}(\mathcal{T}_{fj} < \mathcal{T}^{\mathrm{cut}}) = \sigma_{\geq 0}^{\mathrm{FO,NNLO}} - \sigma_{\geq 1}^{\mathrm{FO,NLO}}(\mathcal{T}_{fj} > \mathcal{T}^{\mathrm{cut}}) \tag{2.25}$$

where $\sigma_{\geq 0}^{\mathrm{FO,NNLO}}$ is the full NNLO Higgs production cross section, and $\sigma_{\geq 1}^{\mathrm{FO,NLO}}(\mathcal{T}_{fj} > \mathcal{T}^{\mathrm{cut}})$ is the NLO $H + j$ cross section with the given cut.

We improve the NNLO nonsingular piece by including the resummation of time-like logarithms in this piece as well. The expression for the final NNLO nonsingular piece that we include is then [2, 7]:

$$\sigma_0^{\text{nons,NNLO}+\pi^2}(\mathcal{T}_{fj} < \mathcal{T}^{\text{cut}}) = \left[\sigma_0^{\text{nons,NNLO}}(\mathcal{T}_{fj} < \mathcal{T}^{\text{cut}}) - \frac{\alpha_s(\mu_{\text{FO}})C_A\pi^2}{2\pi}\sigma_0^{\text{nons,NLO}}(\mathcal{T}_{fj} < \mathcal{T}^{\text{cut}})\right]$$
$$\times\, U_H(m_H^2, -i\mu_{\text{FO}}, \mu_{\text{FO}}) \tag{2.26}$$

In practice, the computation of $\sigma_0^{\text{nons,NNLO}}$ is done with finite m_b, m_t up to NLO, and with $m_b \to 0, m_t \to \infty$ in the NNLO coefficient. This means that in the $\sigma_0^{\text{resum,NNLL}'}$ term of Eq. (2.24) we use a hard function H_{gg} which is given by using Eq. (2.5) but with the $m_t \to \infty$ limit in the NNLO coefficient. The NNLO Higgs cross section is obtained using HNNLO [48–50], whilst the $H+j$ cross section for $\mathcal{T}_{fj} > \mathcal{T}^{\text{cut}}$ is generated using MADGRAPH5_AMC@NLO [27, 51]. The computation of $\sigma_0^{\text{nons,NLO}}$ is done with finite m_t, m_b using similar techniques. This procedure implies that for $\mathcal{T}^{\text{cut}} \to \infty$, we reproduce the NNLO cross section including the resummation of time-like logarithms [20], which is numerically very close to the N^3LO total cross section [52, 53].

3   Profile scales and Perturbative Uncertainties

We now discuss how we choose the beam and soft scales as a function of $\mathcal{T}^{\text{cut}}$, which, following a standard convention for SCET computations, we refer to as the profile scales [54, 55]. At small $\mathcal{T}^{\text{cut}} \ll m_H$, logarithms of $\mathcal{T}^{\text{cut}}/m_H$ are large, Eq. (2.2) applies, and we should set the beam and soft scales to their canonical values $\mu_B \sim \sqrt{m_H\mathcal{T}^{\text{cut}}}, \mu_S \sim \mathcal{T}^{\text{cut}}$ to resum these logarithms appropriately. This is referred to as the resummation region. At large $\mathcal{T}^{\text{cut}} \gtrsim m_H$, we enter the fixed-order region, in which the veto is sufficiently loose that the fixed-order formula applies, and we should set $\mu_B \sim m_H, \mu_S \sim m_H$. In the intermediate region, referred to as the transition region, one should ensure a smooth transition between these two behaviours, which we achieve through a suitable choice of profile scales.

One can determine the locations of the boundaries between these regions by plotting the fixed-order singular and nonsingular contributions to the fixed-order NNLO cross section differential in $\mathcal{T}_{fj}$. The singular piece directly follows from taking the derivative of Eq. (2.2) with respect to $\mathcal{T}^{\text{cut}}$, and contains the leading small $\mathcal{T}_{fj}$ terms $\sim \ln^n(\mathcal{T}_{fj}/m_H)/\mathcal{T}_{fj}$ (corresponding to the $\ln^n(\mathcal{T}^{\text{cut}}/m_H)$ terms in the cumulant). The nonsingular contains the remainder of the NNLO cross section, obtained in practice by subtracting the singular contribution from a NLO $H + j$ computation of the $\mathcal{T}_{fj}$ spectrum from MADGRAPH5_AMC@NLO. At small $\mathcal{T}_{fj}$ this should diverge at most as $\ln^n(\mathcal{T}_{fj}/m_H)$. The resummation region should be defined by where the singular cross section greatly exceeds the nonsingular one, and we should enter the fixed-order region when the singular and nonsingular cross sections become of the same size.

We plot the singular, nonsingular and total NNLO cross sections differential in $\mathcal{T}_{Bj}$ (left) and $\mathcal{T}_{Cj}$ (right) in Fig. 1. One observes that at small $\mathcal{T}_{fj}$ the computed nonsingular contribution indeed has a rather mild dependence on $\mathcal{T}_{fj}$, and does not diverge as strongly as $1/\mathcal{T}_{fj}$;
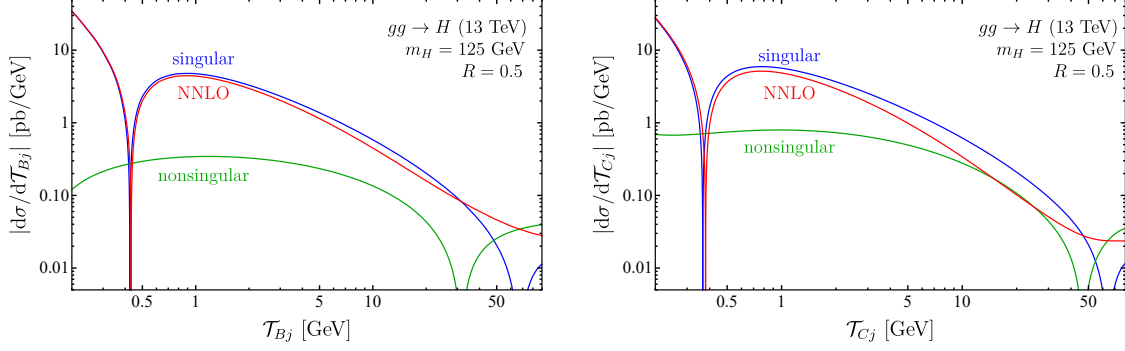
Figure 1. The singular, nonsingular and full fixed order NNLO cross section differential in $\mathcal{T}_{Bj}$ (left) and $\mathcal{T}_{Cj}$ (right) for R=0.5.

this serves as an important cross-check of the two-loop pieces in Eq. (2.2) not proportional to $\delta(\mathcal{T}^{\mathrm{cut}})$, which also appear in the singular spectrum calculation. Towards larger $\mathcal{T}_{fj}$ values, around $\mathcal{T}_{fj} \sim 50$ GeV, the singular and nonsingular contributions become comparable, and for $\mathcal{T}_{fj} \sim 70$ GeV the singular contribution crosses zero. It is interesting to observe that the nonsingular contribution for $\mathcal{T}_{Cj}$ is generally larger than that for $\mathcal{T}_{Bj}$.

Comparing Fig. 1 to Fig. 2 of Ref. [11], we see no particular reason to adjust the boundaries of the resummation, transition and fixed-order regions from the ones chosen in the NLL′+NLO calculation of Ref. [11]. The two boundaries are chosen to be at 18.75 GeV and 75 GeV for $\mathcal{T}_{Bj}$, and at 12.5 GeV and 68.75 GeV for $\mathcal{T}_{Cj}$.

The functional form of the profile scales we use are similar to those adopted in Refs. [7, 11]. In particular, we have:

$$
\begin{aligned}
\mu_H &= -\mathrm{i}\mu_{\mathrm{FO}}\,, \\
\mu_S(\mathcal{T}^{\mathrm{cut}}) &= \mu_{\mathrm{FO}} f_{\mathrm{run}}(\mathcal{T}^{\mathrm{cut}}/m_H)\,, \\
\mu_B(\mathcal{T}^{\mathrm{cut}}) &= \sqrt{\mu_S(\mathcal{T}^{\mathrm{cut}})\mu_{\mathrm{FO}}} = \mu_{\mathrm{FO}}\sqrt{f_{\mathrm{run}}(\mathcal{T}^{\mathrm{cut}}/m_H)}\,,
\end{aligned}
\tag{3.1}
$$

where the profile function $f_{\mathrm{run}}(x)$ is:

$$
f_{\mathrm{run}}(x) = \begin{cases}
x_0\big[1 + (2r_s - 1)(x/x_0)^2/4\big] & x \le 2x_0\,, \\
r_s x & 2x_0 \le x \le x_1\,, \\
r_s x + \frac{(2-r_s x_2 - r_s x_3)(x-x_1)^2}{2(x_2-x_1)(x_3-x_1)} & x_1 \le x \le x_2\,, \\
1 - \frac{(2-r_s x_1 - r_s x_2)(x-x_3)^2}{2(x_3-x_1)(x_3-x_2)} & x_2 \le x \le x_3\,, \\
1 & x_3 \le x\,.
\end{cases}
\tag{3.2}
$$

For $r_s = 1$ the profiles reduce to those of Refs. [7, 11]. For $2x_0 m_H < \mathcal{T}^{\mathrm{cut}} < x_1 m_H$, μ_B and μ_S have canonical scaling: $\mu_S = r_s \mathcal{T}^{\mathrm{cut}}$ and $\mu_B = \sqrt{r_s m_H \mathcal{T}^{\mathrm{cut}}}$ for $\mu_{\mathrm{FO}} = m_H$. The fixed-order region is reached at $\mathcal{T}^{\mathrm{cut}} = x_3 m_H$, with a smooth transition being achieved in two steps between $x_1 m_H$ and $x_3 m_H$. We refer to $\mathcal{T}^{\mathrm{cut}} < 2x_0 m_H$ as the 'nonperturbative region',

and choose $2x_0 m_H$ to be in vicinity of Λ_{QCD}. In this region the variation of $\mu_{S/B}$ is gradually turned off as $\mathcal{T}^{\mathrm{cut}} \to 0$, with μ_S and μ_B approaching the positive values $x_0 \mu_{\mathrm{FO}}$ and $\sqrt{x_0} \mu_{\mathrm{FO}}$ at $\mathcal{T}^{\mathrm{cut}} = 0$. This is to avoid α_s and the PDFs being evaluated at too low scales. In fact our purely perturbative predictions for the cross section will be insufficient in this (small) region, since neglected power corrections can become of $\mathcal{O}(1)$.

For the parameters $x_0 - x_3$ and μ_{FO}, we make the same choices as in Ref. [11], which in particular enforces the same boundaries between resummation, transition and fixed-order regions as in that paper (and which are mentioned above). So, for $\mathcal{T}_{Bj}$ we have:

$$\mu_{\mathrm{FO}} = m_H \,, \qquad x_0 = 2.5 \,\mathrm{GeV}/\mu_{\mathrm{FO}} \,, \ \{x_1, x_2, x_3\} = \{0.15, 0.375, 0.6\} \,, \tag{3.3}$$

and for $\mathcal{T}_{Cj}$,

$$\mu_{\mathrm{FO}} = m_H \,, \qquad x_0 = 2.5 \,\mathrm{GeV}/\mu_{\mathrm{FO}} \,, \qquad \{x_1, x_2, x_3\} = \{0.1, 0.325, 0.55\} \,.$$

The parameter r_s should be chosen to be $\mathcal{O}(1)$. In the next section we will generate results using both $r_s = 1$ and $r_s = 2$.

Let us now move to a discussion of how we estimate the theoretical uncertainty in our predictions of the jet vetoed cross sections. These may be parametrized in terms of fully correlated (yield) and fully anti-correlated (migration) components [2, 7, 56, 57]. The yield uncertainty corresponds to the fixed-order uncertainty Δ_{FO}. At large $\mathcal{T}^{\mathrm{cut}}$ this reproduces the fixed-order scale variation uncertainty in the total inclusive cross section. The migration uncertainty corresponds to the uncertainty in the resummed logarithmic series induced by the jet veto cut and is identified as the resummation uncertainty Δ_{resum}. The total uncertainty in the 0-jet cross section can be written as

$$\Delta_0^2(\mathcal{T}^{\mathrm{cut}}) = \Delta_{\mathrm{FO}}^2(\mathcal{T}^{\mathrm{cut}}) + \Delta_{\mathrm{resum}}^2(\mathcal{T}^{\mathrm{cut}}) \,. \tag{3.4}$$

To estimate these perturbative uncertainties, we vary the profile scales about their central values. For the fixed-order uncertainty Δ_{FO}, we vary μ_{FO} in the range $\{2m_H, m_H/2\}$ in Eq. 3.1, and the resulting profiles are illustrated for the case $r_s = 2$ in the left panel of Fig. 2. The resummation uncertainty Δ_{resum} can be obtained by varying the μ_B and μ_S scales using a multiplicative factor,

$$f_{\mathrm{vary}}(x) = \begin{cases} 2(1 - (1+\delta)x^2/x_3^2) & 0 \le x \le x_3/2 \\ 1 + 2(1-3\delta)(1-x/x_3)^2 + 16\delta(1-x/x_3)^4 & x_3/2 \le x \le x_3 \\ 1 & x_3 \le x \end{cases} \,, \tag{3.5}$$

For $\delta = 0$, this reproduces the functional form of f_{vary} used in Ref. [11]. Here we set $\delta = 0.05$, so that when using $r_s = 2$, we avoid either μ_B or μ_S rising above the fixed-order value of m_H in any of the variations discussed below.
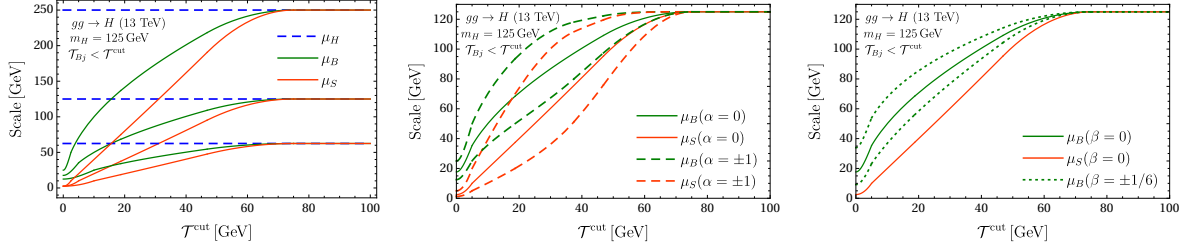
Figure 2. The left panel shows the collective variation of μ_B and μ_S scales by a factor of 2 (using $\mu_{\rm FO} = \{m_H, 2m_H, m_H/2\}$ in Eq. 3.1)) which estimates the fixed order scale uncertainty. The plots in the middle and right panels show μ_B and μ_S variation as discussed in the text (Eq. 3.6), used to estimate the resummation uncertainty. All plots in this figure have been generated using $r_s = 2$ in Eq. (3.2).

The up and down variations of μ_B and μ_S are parametrized using this multiplicative factor as follows,

$$
\mu_S^{\rm vary}(x, \alpha) = f_{\rm vary}^\alpha(x)\, \mu_S(x) = \mu_{\rm FO}\, f_{\rm vary}^\alpha(x)\, f_{\rm run}(x)\,,
$$
$$
\mu_B^{\rm vary}(x, \alpha, \beta) = \mu_S^{\rm vary}(x, \alpha)^{1/2-\beta}\, \mu_{\rm FO}^{1/2+\beta} = \mu_{\rm FO}\big[f_{\rm vary}^\alpha(x)\, f_{\rm run}(x)\big]^{1/2-\beta}\,, \tag{3.6}
$$

with $(\alpha, \beta) = \{(+1, 0), (-1, 0), (0, +1/6), (0, -1/6)\}$. The variations in the parameter α lead to a factor of 2 variation in μ_S for $\mathcal{T}^{\rm cut} \to 0$, and a factor of $\sqrt{2}$ variation in μ_B. The profiles thus obtained with α variation are shown for $r_s = 2$ by the dashed curves in the middle panel of Fig. 2. The parameter β modifies μ_B by varying the canonical relation $\mu_B \sim \sqrt{\mu_S \mu_H}$ while keeping μ_S fixed, as is shown for $r_s = 2$ by the dotted lines in the right panel of Fig. 2. A detailed discussion about the choice of these parameters can be found in Ref. [11]. These variations in μ_S and μ_B vary the arguments of the logarithms in the evolution kernel, and thus help in estimating the higher-order corrections in the resummed results. The total resummation uncertainty $\Delta_{\rm resum}$ is obtained by taking the maximum of the absolute deviation from the central profile.

4 Resummed Predictions at NNLL′+NNLO

In this section we present our results for the 0-jet gluon-fusion Higgs cross section at NNLL′+NNLO with the jet veto imposed via the $\mathcal{T}_{Bj}$ and $\mathcal{T}_{Cj}$ variables. We compare these results to NLL′+NLO and NLL results for the same cross sections, to study the perturbative convergence.

Let us briefly summarise our set-up. For the PDFs we use the MMHT sets [58]: the mmht2014lo135 set for the NLL, the mmht2014nlo120 set for the NLL′+NLO, and the mmht2014nnlo118 set for the NNLL′+NNLO predictions. We take $m_H = 125$ GeV, $m_t = 172.5$ GeV, $m_b = 4.7$ GeV, and set $n_f = 5$ in all perturbative ingredients. The effect of finite m_b, m_t are taken into account in the hard function of the resummation H_{gg} and the nonsingular cross section up to NLO; for the NNLO coefficient of the nonsingular cross section we use
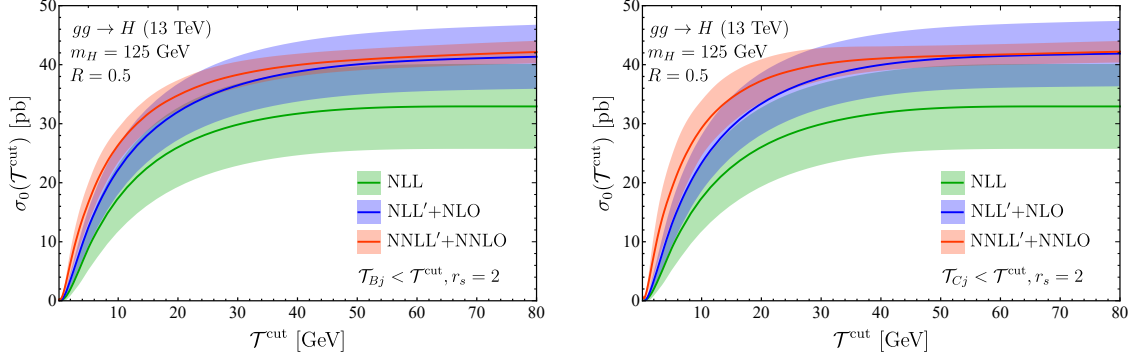
Figure 3. The dark orange band shows the cumulant NNLL′+NNLO cross section for $\mathcal{T}_{Bj} < \mathcal{T}^{\mathrm{cut}}$ (left panel) and $\mathcal{T}_{Cj} < \mathcal{T}^{\mathrm{cut}}$ (right panel) for $R = 0.5$. The blue and green bands correspond to NLL′+NLO and NLL predictions respectively, for each of the two observables. The solid lines indicate the predictions using the central values of the profile scales. These results have been obtained using $r_s = 2$ in Eq. (3.2).
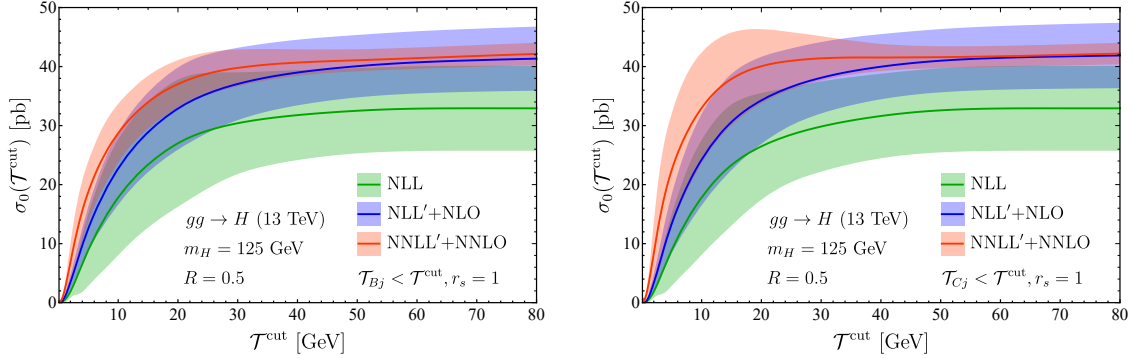

Figure 4. The same plots as in Fig. 3, but now generated setting $r_s = 1$ in Eq. (3.2).

the $m_t \to \infty, m_b \to 0$ result, whereas for the NNLO coefficient of H_{gg} we use the approach described under Eq. (2.5). The central prediction has $i\mu_H = \mu_{\mathrm{FO}} = m_H$ and μ_B, μ_S defined by the profile functions in Eq. (3.1). The uncertainty bands are estimated using profile scale variations as discussed in Sec. 3.

We plot the cross section with $\mathcal{T}_{B/Cj} < \mathcal{T}^{\mathrm{cut}}$ as a function of $\mathcal{T}^{\mathrm{cut}}$, for two choices of r_s in Eq. (3.2): $r_s = 1$ and $r_s = 2$. In each case we make plots using both a linear and a logarithmic x-axis. The results for $r_s = 2$ are given in Fig. 3 and Fig. 5, and those for $r_s = 1$ are given in Fig. 4 and Fig. 6. In each figure, we plot our NNLL′+NNLO results in orange, and give NLL′+NLO and NLL results in blue and green respectively.

In general, we see a substantial reduction of uncertainties going from NLL′ to NNLL′, due to the increase in the accuracy of resummation as well as matching. The predictions of higher orders fall within the uncertainty bands of lower orders, thereby indicating a good
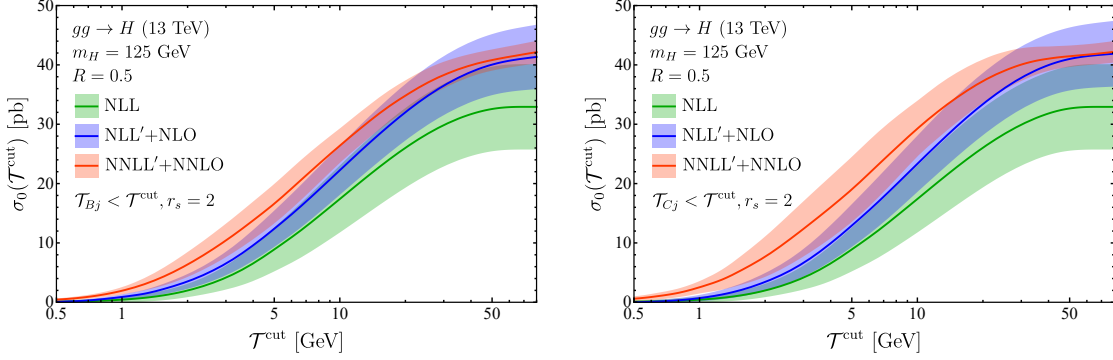
Figure 5. The same plots as in Fig. 3, but with a logarithmic x-axis.
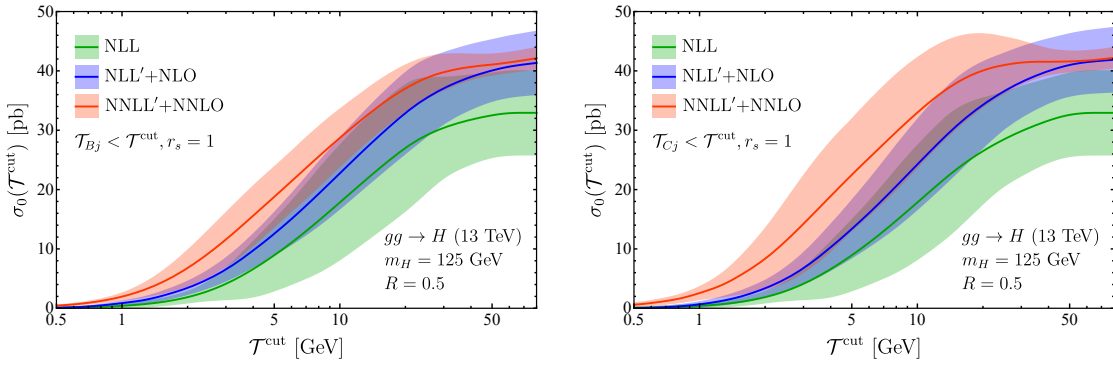

Figure 6. The same plots as in Fig. 4, but with a logarithmic x-axis.

perturbative convergence.

Comparing the results with $r_s = 2$ to those with $r_s = 1$, we see a better convergence between different orders in resummed perturbation theory in the former case, where this is particularly noticeable for $\mathcal{T}_{Cj}$. In the case of $\mathcal{T}_{Cj}$ with $r_s = 1$, one also observes that the top of the uncertainty band at $\mathcal{T}^{\text{cut}} \sim 20$ GeV greatly exceeds that of the total NNLO cross section. This is of course unphysical. For these reasons we would advocate to use the results with $r_s = 2$ for $\mathcal{T}_{Cj}$. The choice of $r_s = 2$, corresponding to the choice of canonical scale $\mu_S = 2\mathcal{T}^{\text{cut}}$, also seems physically reasonable for $\mathcal{T}_{Cj}$, since the cut $\mathcal{T}_{Cj} < \mathcal{T}^{\text{cut}}$ corresponds to an m_{Tj} cut that is everywhere looser than $m_{Tj} < 2\mathcal{T}^{\text{cut}}$. For the case of $\mathcal{T}_{Bj}$, there is not a strong difference between the $r_s = 1$ or $r_s = 2$ results and one can use either of these.

We note in passing that similar conclusions with regards to the scales in the resummation region were also found for thrust and C-parameter in e^+e^- collisions, in Ref. [39]. Furthermore, we note that in Ref. [2], where NNLL+NNLO predictions were obtained for Higgs production with a cut on beam thrust (the global equivalent of $\mathcal{T}_{Bj}$), profile scales that are rather close to $\mu_S = 2\mathcal{T}^{\text{cut}}, \mu_B = \sqrt{m_H \mu_S}$ in the resummation region were used.

Finally, in Table 1 we present numbers for the $H+0$-jet cross section defined by $\mathcal{T}_{B/Cj} <$

$\mathcal{T}^{\mathrm{cut}}$, at two sample values of $\mathcal{T}^{\mathrm{cut}}$: 20 GeV and 30 GeV. We give the central predictions and perturbative uncertainties, for both the $r_s = 1$ and $r_s = 2$ cases.

These numbers highlight the improvement in perturbative convergence going from $r_s = 1$ to $r_s = 2$ that was already visible in Figs. 3 - 6. For the results with $r_s = 2$, the perturbative uncertainties are smaller compared to the results with $r_s = 1$, and the NNLL′+NNLO results lie closer to the NLL′+NLO ones for $r_s = 2$. We again see that this is more pronounced for the $\mathcal{T}_{Cj}$ case, leading to the choice $r_s = 1$ being disfavoured for $\mathcal{T}_{Cj}$.

	$\sigma_0(\mathcal{T}^{\mathrm{cut}})[\mathrm{pb}]\ (r_s = 1)$	$\sigma_0(\mathcal{T}^{\mathrm{cut}})[\mathrm{pb}]\ (r_s = 2)$
NLL′+NLO		
$\mathcal{T}_{Bj} < \mathcal{T}^{\mathrm{cut}} = 20\,\mathrm{GeV}$	$32.88 \pm 6.95\,(21.2\%)$	$32.02 \pm 4.75\,(14.8\%)$
$\mathcal{T}_{Bj} < \mathcal{T}^{\mathrm{cut}} = 30\,\mathrm{GeV}$	$37.05 \pm 6.12\,(16.5\%)$	$36.50 \pm 4.96\,(13.6\%)$
NNLL′+NNLO		
$\mathcal{T}_{Bj} < \mathcal{T}^{\mathrm{cut}} = 20\,\mathrm{GeV}$	$37.03 \pm 4.06\,(10.9\%)$	$34.81 \pm 2.57\,(7.39\%)$
$\mathcal{T}_{Bj} < \mathcal{T}^{\mathrm{cut}} = 30\,\mathrm{GeV}$	$39.77 \pm 3.11\,(7.82\%)$	$38.30 \pm 2.23\,(5.82\%)$
NLL′+NLO		
$\mathcal{T}_{Cj} < \mathcal{T}^{\mathrm{cut}} = 20\,\mathrm{GeV}$	$34.28 \pm 7.37\,(21.5\%)$	$33.40 \pm 5.24\,(15.7\%)$
$\mathcal{T}_{Cj} < \mathcal{T}^{\mathrm{cut}} = 30\,\mathrm{GeV}$	$38.10 \pm 6.05\,(15.8\%)$	$37.82 \pm 5.27\,(13.9\%)$
NNLL′+NNLO		
$\mathcal{T}_{Cj} < \mathcal{T}^{\mathrm{cut}} = 20\,\mathrm{GeV}$	$40.05 \pm 6.28\,(15.69\%)$	$37.27 \pm 3.64\,(9.77\%)$
$\mathcal{T}_{Cj} < \mathcal{T}^{\mathrm{cut}} = 30\,\mathrm{GeV}$	$41.39 \pm 3.75\,(9.07\%)$	$40.05 \pm 2.75\,(6.88\%)$

Table 1. Predictions for the $\mathcal{T}_{Bj}$ and $\mathcal{T}_{Cj}$ $H + 0$-jet cross sections obtained using the central profile scales, along with the total perturbative uncertainties. The equivalent percentage uncertainties are shown in brackets.

5 Effect of underlying event and hadronisation

The analytic resummed calculations presented in the previous section do not take into account the effects of underlying event or hadronisation. These effects are formally suppressed, but it is interesting to assess their practical numerical impact, and compare how much $\mathcal{T}_{B/Cj}$ are affected with respect to the conventional jet veto observable p_{Tj}.

In order to do this, we employ a NLO + parton shower set-up, as implemented in MAD-GRAPH5_AMC@NLO interfaced with Pythia8. In Pythia8, the parameters have been set to their default values as specified by the MADGRAPH5_AMC@NLO interface. These parameter values mainly correspond to the Monash 2013 tune [59] – in particular the underlying event and hadronisation parameters are set as in this tune. We generate ggF Higgs events, compute the cumulant distributions for $\mathcal{T}_{Bj}$, $\mathcal{T}_{Cj}$ and p_{Tj} from these events, and investigate the effect of turning on and off hadronisation and underlying event (UE) in the shower on
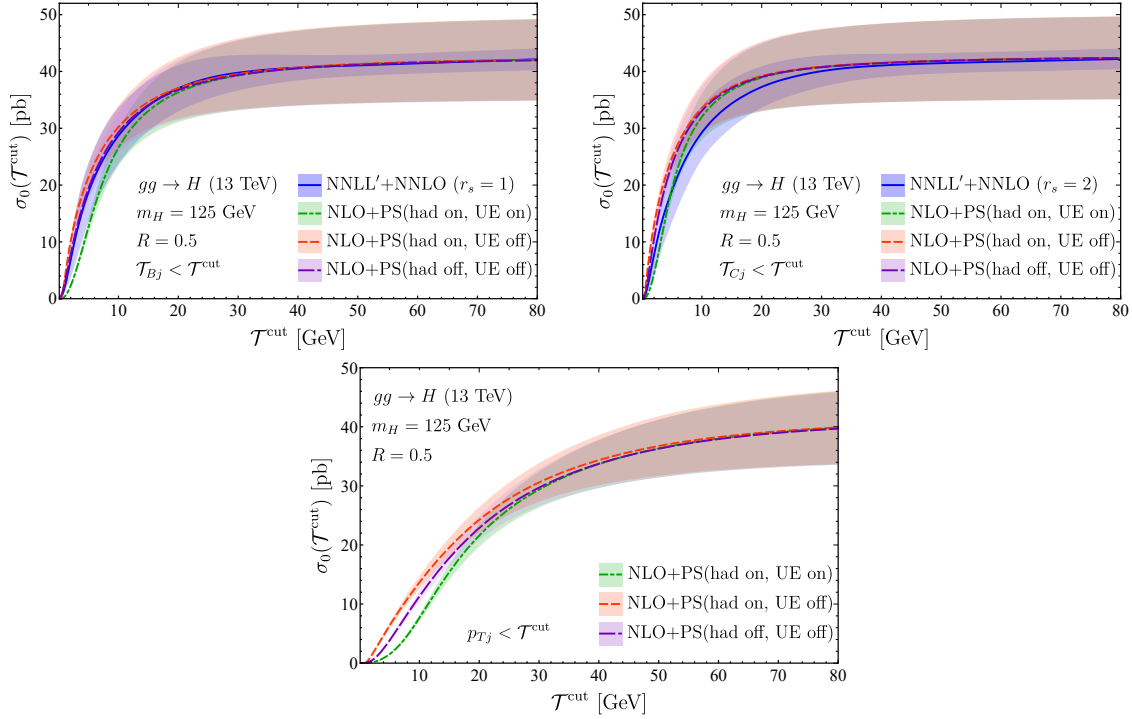
Figure 7. NLO + parton shower results for the Higgs cross section for $\mathcal{T}_{B/Cj}, p_{Tj} < \mathcal{T}^{\mathrm{cut}}$ and $R = 0.5$, generated using MadGraph5_aMC@NLO interfaced with Pythia8. The overall normalisation of these predictions has been adjusted such that the central predictions reproduce the NNLO Higgs cross section (including resummation of time-like logarithms) for $\mathcal{T}^{\mathrm{cut}} \to \infty$. The green, red and purple bands represent various configurations with regards to the hadronisation and underlying event. For the $\mathcal{T}_{B/Cj}$ cases, we also plot in blue the NNLL′+NNLO analytic prediction for comparison.

these cumulant distributions. Jets with $R = 0.5$ are identified in the events using the anti-k_T algorithm [60].

In Fig. 7, we give the NLO+PS plots for all jet vetoes, for three configurations of the parton shower: hadronisation and UE turned on, hadronisation on and UE off, and both hadronisation and UE turned off. Fig. 8 presents the same plots, but with a logarithmic x-axis. For the $\mathcal{T}_{B/Cj}$ cases, we also give the NNLL′+NNLO prediction, using the same set-up as in section 4 and taking $r_s = 1$ ($r_s = 2$) for $\mathcal{T}_{Bj}$ ($\mathcal{T}_{Cj}$). To allow for a meaningful comparison, we rescale all NLO+PS predictions to the total cross section of our NNLL′+NNLO predictions. The uncertainty bands on the NLO+PS results reflect the (rescaled) fixed-order scale variation.

From these plots, one can see that hadronisation tends to shift the p_{Tj} and $\mathcal{T}_{B/Cj}$ distributions towards lower values, whilst UE pushes these distributions towards higher values. Non-perturbative hadronisation 'smears out' the energy in QCD particle sprays over a larger area in $\eta - \phi$ phase space, resulting in a loss of p_{Tj} and $\mathcal{T}_{B/Cj}$ from any given jet with fixed R. UE sprays extra particles fairly evenly over the $\eta - \phi$ phase space, with these extra particles
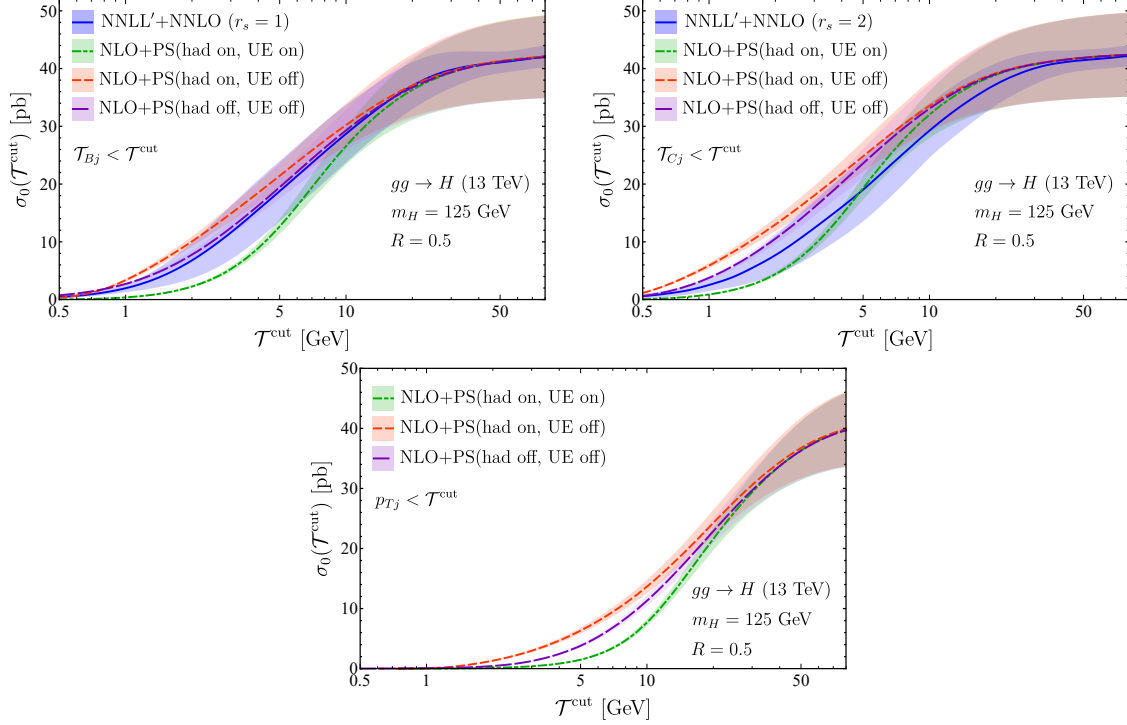
Figure 8. The same plots as in Fig. 7, but with a logarithmic x-axis.

pushing up the p_{Tj} and $\mathcal{T}_{B/Cj}$ values of all jets [61].

One can also already see from these plots that the cross section with a p_{Tj} veto is more strongly affected by hadronisation and UE effects than those with $\mathcal{T}_{Bj}$ and $\mathcal{T}_{Cj}$ vetoes. Finally, it is interesting to note that the rescaled NLO+PS predictions for $\mathcal{T}_{Bj}$ and $\mathcal{T}_{Cj}$ turn out to lie fairly close to the NNLL$'$+NNLO predictions.

In order to exhibit in more detail the extent to which all three vetoed cross sections are sensitive to UE and hadronisation, we plot in Fig. 9 the following ratios:

$$\mathcal{R}_{(\text{UE/no UE})}(\mathcal{T}^{\text{cut}}) = \frac{\sigma_0\left(\mathcal{T}^{\text{cut}}\right)\big|_{\text{had on, UE on}}}{\sigma_0\left(\mathcal{T}^{\text{cut}}\right)\big|_{\text{had on, UE off}}} \tag{5.1}$$

$$\mathcal{R}_{(\text{no had/had})}(\mathcal{T}^{\text{cut}}) = \frac{\sigma_0\left(\mathcal{T}^{\text{cut}}\right)\big|_{\text{had off, UE off}}}{\sigma_0\left(\mathcal{T}^{\text{cut}}\right)\big|_{\text{had on, UE off}}} \tag{5.2}$$

The first ratio indicates the extent to which each observable is sensitive to UE, and the second indicates the extent to which each observable is sensitive to hadronisation. The closer the $\mathcal{R}$ value is to 1, the lower the sensitivity is. For p_{Tj} and $\mathcal{T}_{Bj}$, the cumulant cross sections $\sigma_0\left(\mathcal{T}^{\text{cut}}\right)$ are computed by integrating p_{Tj} or $\mathcal{T}_{Bj}$ up to $\mathcal{T}^{\text{cut}}$ as before, whilst for $\mathcal{T}_{Cj}$ we integrate up to $\mathcal{T}^{\text{cut}}/2$. We do this so that at a given point on the x-axis in Fig. 9 all the different veto observables correspond to the same 'central' p_{Tj} veto at $y_j = Y$ in the limit of small jet radius R (namely, $p_{Tj}\big|_{y_j=Y, R \ll 1} < \mathcal{T}^{\text{cut}}$).
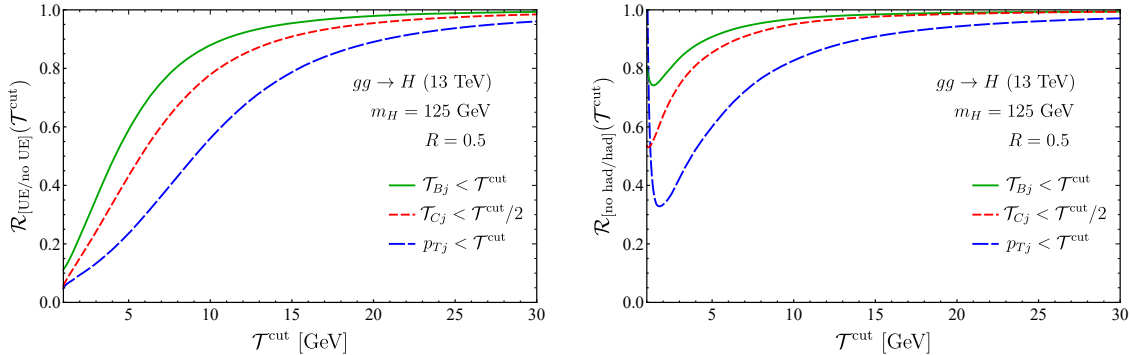
Figure 9. Plots for the ratios $\mathcal{R}_{(\text{UE/no UE})}(\mathcal{T}^{\text{cut}})$ and $\mathcal{R}_{(\text{no had/had})}(\mathcal{T}^{\text{cut}})$ defined in Eqs. (5.1) and (5.2).

These results confirm that the cross sections with $\mathcal{T}_{Bj}$ and $\mathcal{T}_{Cj}$ vetoes are less sensitive to UE and hadronisation effects than that with the p_{Tj} veto, and show that the cross section with the $\mathcal{T}_{Bj}$ veto is less sensitive than that with the $\mathcal{T}_{Cj}$ veto for the same central p_{Tj} veto. Reduced sensitivity is of course advantageous, given that our current theoretical description of these effects is based on models rather than first principles theory.

This ordering of sensitivities to UE and hadronisation effects actually makes intuitive sense. The rapidity-dependent vetoes $\mathcal{T}_{B/Cj}$ impose a similar veto as p_{Tj} at $y_j = Y$, but as one moves away from the Higgs rapidity and $|y_j - Y|$ increases, the veto is lifted and one moves towards simply measuring the inclusive Higgs cross section in these forward regions. The inclusive Higgs cross section is, of course, much less affected by hadronisation and UE than the cross section with a restriction on p_{Tj}, and this leads to the cross sections with a $\mathcal{T}_{B/Cj}$ veto being less sensitive to UE and hadronisation than that with a p_{Tj} veto. With the same 'central' p_{Tj} veto at $y_j = Y$, the veto is lifted more quickly as one goes forward in rapidity for $\mathcal{T}_{Bj}$ than $\mathcal{T}_{Cj}$ (see Fig. 1 of Ref. [11]), and this leads to the cross section with a $\mathcal{T}_{Bj}$ veto being less sensitive to UE and hadronisation than the cross section with a $\mathcal{T}_{Cj}$ veto.

6 Conclusions

In this paper, we obtained NNLL$'$+NNLO predictions for the 0-jet gluon-fusion Higgs cross section, $\sigma_0(\mathcal{T}^{\text{cut}})$, where the jet veto is imposed by requiring that no identified jet has a value of $\mathcal{T}_{B/Cj}$ greater than $\mathcal{T}^{\text{cut}}$. The observables $\mathcal{T}_{Bj}$ and $\mathcal{T}_{Cj}$, defined in Eq. (1.1), correspond to a rapidity-dependent jet veto: they impose the tightest constraint on jet transverse mass at 'central' rapidities close to the Higgs rapidity, with the veto gradually loosening as one goes to forward rapidities away from the Higgs. The perturbative uncertainty in these predictions has been estimated through combined scale variations of the different resummation and fixed-order scales involved. We compared the NNLL$'$+NNLO predictions to lower-order NLL and NLL$'$+NLO ones, observing in general that the perturbative uncertainties significantly reduce as the perturbative order is increased, and that the predictions of higher orders fall within the

uncertainty bands of lower orders, indicating good perturbative convergence. Explicit results have been provided for jet radius $R = 0.5$, but results for other jet radii can be provided on request to the authors.

In the 'resummation region' $\mathcal{T}^{\text{cut}} \ll m_H$, the soft and beam resummation scales μ_S and μ_B in our predictions should be chosen to be $r_s \mathcal{T}^{\text{cut}}$ and $\sqrt{r_s m_H \mathcal{T}^{\text{cut}}}$ respectively, where r_s is some number of order 1. We investigated the use of both $r_s = 1$ and $r_s = 2$. Whilst for $\mathcal{T}_{Bj}$ the $r_s = 1$ and $r_s = 2$ predictions look rather similar, for $\mathcal{T}_{Cj}$ use of $r_s = 2$ notably improves the perturbative convergence and avoids an unphysical behaviour in the jet-vetoed cross section. For these reasons, we advocate the use of our $r_s = 2$ results for $\mathcal{T}_{Cj}$. Taking $r_s = 2$ for $\mathcal{T}_{Cj}$, we find, setting $\mathcal{T}^{\text{cut}}$ to the benchmark value of 20 GeV and R to 0.5, that the perturbative uncertainty on the vetoed cross section reduces from 15.7% at NLL$'$+NLO to 9.77% at NNLL$'$+NNLO, with the central value increasing from 33.4 pb to 37.3 pb. Repeating the exercise with $\mathcal{T}_{Bj}$ and taking $r_s = 1$, we find a reduction in uncertainty from 21.2% to 10.9%, with the central value increasing from 32.9 pb to 37.0 pb.

Using an NLO+PS set-up, we compared the effect of underlying event (UE) and hadronisation on 0-jet ggH cross sections where the jet veto constraint was implemented via $\mathcal{T}_{Bj}$, $\mathcal{T}_{Cj}$ or the conventional jet veto observable p_{Tj}. Adjusting all three vetoes such that they imposed the same jet veto at central rapidities (at small R), we found that the cross-section with the $\mathcal{T}_{Bj}$ veto was minimally sensitive to both UE and hadronisation, followed by that with $\mathcal{T}_{Cj}$, and then finally the cross section with the p_{Tj} veto was the most sensitive. The fact that the cross sections with rapidity-dependent jet vetoes have a reduced sensitivity to these theoretically less-well-understood effects is one advantage of using such vetoes.

The use of $\mathcal{T}_{B/Cj}$ rather than p_{Tj} to classify and veto jets has practical advantages, and also provides complementary information on the properties of additional jet production in a given hard process. We look forward to comparing our predictions for 0-jet ggH cross sections with a $\mathcal{T}_{B/Cj}$ veto against data from the LHC experiments.

Acknowledgments

References

[1] I. W. Stewart, F. J. Tackmann and W. J. Waalewijn, *Factorization at the LHC: From PDFs to Initial State Jets*, *Phys. Rev.* **D81** (2010) 094035, [0910.0467].

[2] C. F. Berger, C. Marcantonini, I. W. Stewart, F. J. Tackmann and W. J. Waalewijn, *Higgs Production with a Central Jet Veto at NNLL+NNLO*, *JHEP* **04** (2011) 092, [1012.4480].

[3] A. Banfi, G. P. Salam and G. Zanderighi, *NLL+NNLO predictions for jet-veto efficiencies in Higgs-boson and Drell-Yan production*, *JHEP* **06** (2012) 159, [1203.5773].

[4] A. Banfi, P. F. Monni, G. P. Salam and G. Zanderighi, *Higgs and Z-boson production with a jet veto*, *Phys. Rev. Lett.* **109** (2012) 202001, [1206.4998].

[5] T. Becher and M. Neubert, *Factorization and NNLL Resummation for Higgs Production with a Jet Veto*, *JHEP* **07** (2012) 108, [1205.3806].

[6] T. Becher, M. Neubert and L. Rothen, *Factorization and N^3LL_p+NNLO predictions for the Higgs cross section with a jet veto*, *JHEP* **10** (2013) 125, [1307.0025].

[7] I. W. Stewart, F. J. Tackmann, J. R. Walsh and S. Zuberi, *Jet p_T resummation in Higgs production at $NNLL' + NNLO$*, *Phys. Rev.* **D89** (2014) 054001, [1307.1808].

[8] A. Banfi, F. Caola, F. A. Dreyer, P. F. Monni, G. P. Salam, G. Zanderighi et al., *Jet-vetoed Higgs cross section in gluon fusion at N^3LO+NNLL with small-R resummation*, *JHEP* **04** (2016) 049, [1511.02886].

[9] J. K. L. Michel, P. Pietrulewicz and F. J. Tackmann, *Jet Veto Resummation with Jet Rapidity Cuts*, *JHEP* **04** (2019) 142, [1810.12911].

[10] F. J. Tackmann, J. R. Walsh and S. Zuberi, *Resummation Properties of Jet Vetoes at the LHC*, *Phys. Rev.* **D86** (2012) 053011, [1206.4312].

[11] S. Gangal, M. Stahlhofen and F. J. Tackmann, *Rapidity-Dependent Jet Vetoes*, *Phys. Rev.* **D91** (2015) 054023, [1412.4792].

[12] I. W. Stewart, F. J. Tackmann and W. J. Waalewijn, *The Beam Thrust Cross Section for Drell-Yan at NNLL Order*, *Phys. Rev. Lett.* **106** (2011) 032001, [1005.4060].

[13] ATLAS collaboration, G. Aad et al., *Measurements of fiducial and differential cross sections for Higgs boson production in the diphoton decay channel at $\sqrt{s} = 8$ TeV with ATLAS*, *JHEP* **09** (2014) 112, [1407.4222].

[14] S. Gangal, J. R. Gaunt, M. Stahlhofen and F. J. Tackmann, *Two-Loop Beam and Soft Functions for Rapidity-Dependent Jet Vetoes*, *JHEP* **02** (2017) 026, [1608.01999].

[15] G. Parisi, *Summing Large Perturbative Corrections in QCD*, *Phys. Lett.* **90B** (1980) 295–296.

[16] G. F. Sterman, *Summation of Large Corrections to Short Distance Hadronic Cross-Sections*, *Nucl. Phys.* **B281** (1987) 310–364.

[17] L. Magnea and G. F. Sterman, *Analytic continuation of the Sudakov form-factor in QCD*, *Phys. Rev.* **D42** (1990) 4222–4227.

[18] V. Ahrens, T. Becher, M. Neubert and L. L. Yang, *Origin of the Large Perturbative Corrections to Higgs Production at Hadron Colliders*, *Phys. Rev.* **D79** (2009) 033013, [0808.3008].

[19] V. Ahrens, T. Becher, M. Neubert and L. L. Yang, *Renormalization-Group Improved Prediction for Higgs Production at Hadron Colliders*, *Eur. Phys. J.* **C62** (2009) 333–353, [0809.4283].

[20] M. A. Ebert, J. K. L. Michel and F. J. Tackmann, *Resummation Improved Rapidity Spectrum for Gluon Fusion Higgs Production*, *JHEP* **05** (2017) 088, [1702.00794].

[21] M. Dasgupta, F. Dreyer, G. P. Salam and G. Soyez, *Small-radius jets to all orders in QCD*, *JHEP* **04** (2015) 039, [1411.5182].

[22] Z.-B. Kang, F. Ringer and I. Vitev, *The semi-inclusive jet function in SCET and small radius resummation for inclusive jet production*, *JHEP* **10** (2016) 125, [1606.06732].

[23] L. Dai, C. Kim and A. K. Leibovich, *Fragmentation of a Jet with Small Radius*, *Phys. Rev.* **D94** (2016) 114023, [1606.07411].

[24] K. Melnikov and A. Penin, *On the light quark mass effects in Higgs boson production in gluon fusion*, *JHEP* **05** (2016) 172, [1602.09020].

[25] T. Liu and A. Penin, *High-Energy Limit of Mass-Suppressed Amplitudes in Gauge Theories*, *JHEP* **11** (2018) 158, [1809.04950].

[26] Z. L. Liu and M. Neubert, *Factorization at Subleading Power and Endpoint-Divergent Convolutions in $h \to \gamma\gamma$ Decay*, 1912.08818.

[27] J. Alwall, R. Frederix, S. Frixione, V. Hirschi, F. Maltoni, O. Mattelaer et al., *The automated computation of tree-level and next-to-leading order differential cross sections, and their matching to parton shower simulations*, *JHEP* **07** (2014) 079, [1405.0301].

[28] T. Sjöstrand, S. Ask, J. R. Christiansen, R. Corke, N. Desai, P. Ilten et al., *An Introduction to PYTHIA 8.2*, *Comput. Phys. Commun.* **191** (2015) 159–177, [1410.3012].

[29] R. Harlander and P. Kant, *Higgs production and decay: Analytic results at next-to-leading order QCD*, *JHEP* **12** (2005) 015, [hep-ph/0509189].

[30] C. Anastasiou, S. Beerli, S. Bucherer, A. Daleo and Z. Kunszt, *Two-loop amplitudes and master integrals for the production of a Higgs boson via a massive quark and a scalar-quark loop*, *JHEP* **01** (2007) 082, [hep-ph/0611236].

[31] A. Pak, M. Rogal and M. Steinhauser, *Virtual three-loop corrections to Higgs boson production in gluon fusion for finite top quark mass*, *Phys. Lett.* **B679** (2009) 473–477, [0907.2998].

[32] R. V. Harlander and K. J. Ozeren, *Top mass effects in Higgs production at next-to-next-to-leading order QCD: Virtual corrections*, *Phys. Lett.* **B679** (2009) 467–472, [0907.2997].

[33] I. W. Stewart, F. J. Tackmann and W. J. Waalewijn, *The Quark Beam Function at NNLL*, *JHEP* **09** (2010) 005, [1002.2213].

[34] J. Gaunt, M. Stahlhofen and F. J. Tackmann, *The Gluon Beam Function at Two Loops*, *JHEP* **08** (2014) 020, [1405.1044].

[35] R. Kelley, M. D. Schwartz, R. M. Schabinger and H. X. Zhu, *The two-loop hemisphere soft function*, *Phys. Rev.* **D84** (2011) 045022, [1105.3676].

[36] P. F. Monni, T. Gehrmann and G. Luisoni, *Two-Loop Soft Corrections and Resummation of the Thrust Distribution in the Dijet Region*, *JHEP* **08** (2011) 010, [1105.4560].

[37] A. Hornig, C. Lee, I. W. Stewart, J. R. Walsh and S. Zuberi, *Non-global Structure of the $O(\alpha_s^2)$ Dijet Soft Function*, *JHEP* **08** (2011) 054, [1105.4628].

[38] J. Gaunt, M. Stahlhofen, F. J. Tackmann and J. R. Walsh, *N-jettiness Subtractions for NNLO QCD Calculations*, *JHEP* **09** (2015) 058, [1505.04794].

[39] A. H. Hoang, D. W. Kolodrubetz, V. Mateu and I. W. Stewart, *C-parameter distribution at N^3LL including power corrections*, *Phys. Rev.* **D91** (2015) 094017, [1411.6633].

[40] G. Bell, R. Rahn and J. Talbert, *Automated Calculation of Dijet Soft Functions in the Presence of Jet Clustering Effects*, *PoS* **RADCOR2017** (2018) 047, [`1801.04877`].

[41] G. Bell, R. Rahn and J. Talbert, *Two-loop anomalous dimensions of generic dijet soft functions*, *Nucl. Phys.* **B936** (2018) 520–541, [`1805.12414`].

[42] G. Bell, R. Rahn and J. Talbert, *Generic dijet soft functions at two-loop order: correlated emissions*, *JHEP* **07** (2019) 101, [`1812.08690`].

[43] S. Moch, J. A. M. Vermaseren and A. Vogt, *The Three loop splitting functions in QCD: The Nonsinglet case*, *Nucl. Phys.* **B688** (2004) 101–134, [`hep-ph/0403192`].

[44] G. P. Korchemsky and A. V. Radyushkin, *Renormalization of the Wilson Loops Beyond the Leading Order*, *Nucl. Phys.* **B283** (1987) 342–364.

[45] A. Idilbi, X.-d. Ji, J.-P. Ma and F. Yuan, *Threshold resummation for Higgs production in effective field theory*, *Phys. Rev.* **D73** (2006) 077501, [`hep-ph/0509294`].

[46] S. Moch, J. A. M. Vermaseren and A. Vogt, *Three-loop results for quark and gluon form-factors*, *Phys. Lett.* **B625** (2005) 245–252, [`hep-ph/0508055`].

[47] A. Idilbi, X.-d. Ji and F. Yuan, *Resummation of threshold logarithms in effective field theory for DIS, Drell-Yan and Higgs production*, *Nucl. Phys.* **B753** (2006) 42–68, [`hep-ph/0605068`].

[48] S. Catani and M. Grazzini, *An NNLO subtraction formalism in hadron collisions and its application to Higgs boson production at the LHC*, *Phys. Rev. Lett.* **98** (2007) 222002, [`hep-ph/0703012`].

[49] M. Grazzini, *NNLO predictions for the Higgs boson signal in the $H \to WW \to l\nu l\nu$ and $H \to ZZ \to 4l$ decay channels*, *JHEP* **02** (2008) 043, [`0801.3232`].

[50] M. Grazzini and H. Sargsyan, *Heavy-quark mass effects in Higgs boson production at the LHC*, *JHEP* **09** (2013) 129, [`1306.4581`].

[51] V. Hirschi and O. Mattelaer, *Automated event generation for loop-induced processes*, *JHEP* **10** (2015) 146, [`1507.00020`].

[52] C. Anastasiou, C. Duhr, F. Dulat, E. Furlan, T. Gehrmann, F. Herzog et al., *High precision determination of the gluon fusion Higgs boson cross-section at the LHC*, *JHEP* **05** (2016) 058, [`1602.00695`].

[53] B. Mistlberger, *Higgs boson production at hadron colliders at N^3LO in QCD*, *JHEP* **05** (2018) 028, [`1802.00833`].

[54] Z. Ligeti, I. W. Stewart and F. J. Tackmann, *Treating the b quark distribution function with reliable uncertainties*, *Phys. Rev.* **D78** (2008) 114014, [`0807.1926`].

[55] R. Abbate, M. Fickinger, A. H. Hoang, V. Mateu and I. W. Stewart, *Thrust at N^3LL with Power Corrections and a Precision Global Fit for $\alpha_s(m_Z)$*, *Phys. Rev.* **D83** (2011) 074021, [`1006.3080`].

[56] I. W. Stewart and F. J. Tackmann, *Theory Uncertainties for Higgs and Other Searches Using Jet Bins*, *Phys. Rev.* **D85** (2012) 034011, [`1107.2117`].

[57] S. Gangal and F. J. Tackmann, *Next-to-leading-order uncertainties in Higgs+2 jets from gluon fusion*, *Phys. Rev.* **D87** (2013) 093008, [`1302.5437`].

[58] L. A. Harland-Lang, A. D. Martin, P. Motylinski and R. S. Thorne, *Parton distributions in the LHC era: MMHT 2014 PDFs*, *Eur. Phys. J.* **C75** (2015) 204, [1412.3989].

[59] P. Skands, S. Carrazza and J. Rojo, *Tuning PYTHIA 8.1: the Monash 2013 Tune*, *Eur. Phys. J.* **C74** (2014) 3024, [1404.5630].

[60] M. Cacciari, G. P. Salam and G. Soyez, *The anti-k_t jet clustering algorithm*, *JHEP* **04** (2008) 063, [0802.1189].

[61] M. Dasgupta, L. Magnea and G. P. Salam, *Non-perturbative QCD effects in jets at hadron colliders*, *JHEP* **02** (2008) 055, [0712.3014].